Modelling and validation of diffuse reflectance of the adult human head for fNIRS: scalp sub-layers definition

Javier Herrera-Vega, Samuel Montero-Hernández, Ilias Tachtsidis, Carlos G. Treviño-Palacios, Felipe Orihuela-Espina

Javier Herrera-Vega, Samuel Montero-Hernández, Ilias Tachtsidis, Carlos G. Treviño-Palacios, Felipe Orihuela-Espina, "Modelling and validation of diffuse reflectance of the adult human head for fNIRS: scalp sub-layers definition," Proc. SPIE 10572, 13th International Conference on Medical Information Processing and Analysis, 1057206 (17 November 2017); doi: 10.1117/12.2285918

SPIE.

Event: 13th International Symposium on Medical Information Processing and Analysis, 2017, San Andres Island, Colombia

Modelling and Validation of Diffuse Reflectance of the Adult Human Head for fNIRS: Scalp sub-layers Definition

Javier Herrera-Vega[a], Samuel Montero-Hernández[a], Ilias Tachtsidis[b], Carlos G. Treviño-Palacios[a], and Felipe Orihuela-Espina[a]

[a]Instituto Nacional de Astrofsica Óptica y Electrónica, Luis Enrique Erro 1, Puebla, México
[b]University College London, Gower Street, London, UK

ABSTRACT

Accurate estimation of brain haemodynamics parameters such as cerebral blood flow and volume as well as oxygen consumption i.e. metabolic rate of oxygen, with funcional near infrared spectroscopy (fNIRS) requires precise characterization of light propagation through head tissues. An anatomically realistic forward model of the human adult head with unprecedented detailed specification of the 5 scalp sublayers to account for blood irrigation in the connective tissue layer is introduced. The full model consists of 9 layers, accounts for optical properties ranging from 750nm to 950nm and has a voxel size of 0.5mm. The whole model is validated comparing the predicted remitted spectra, using Monte Carlo simulations of radiation propagation with 10^8 photons, against continuous wave (CW) broadband fNIRS experimental data. As the true oxy- and deoxy-hemoglobin concentrations during acquisition are unknown, a genetic algorithm searched for the vector of parameters that generates a modelled spectrum that optimally fits the experimental spectrum. Differences between experimental and model predicted spectra was quantified using the Root mean square error (RMSE). RMSE was 0.071 ± 0.004, 0.108 ± 0.018 and 0.235 ± 0.015 at 1, 2 and 3cm interoptode distance respectively. The parameter vector of absolute concentrations of haemoglobin species in scalp and cortex retrieved with the genetic algorithm was within histologically plausible ranges. The new model capability to estimate the contribution of the scalp blood flow shall permit incorporating this information to the regularization of the inverse problem for a cleaner reconstruction of brain hemodynamics.

Keywords: fNIRS, forward model, genetic algorithm, validation

1. INTRODUCTION

Continuous wave functional Near Infrared Spectroscopy (fNIRS) non invasively interrogates local changes in brain hemodynamics. It irradiates the subject's scalp with a continuous pulse of infrared light and collects backscattered light after it has migrated through and interacted with the tissue; a physical process known as *image formation*. Light interaction with chromophores and scatterers present in the head tissues leaves a spectroscopic attenuation signature in the exiting radiation from where the concentration of the chromophores can be estimated; a mathematical effort known as *image reconstruction*. Formation and reconstruction go hand in hand, with the latter involving the inverse problem of unravelling what nature entangled. Like in many other inverse problems, a forward model hypothesizes how the image formation occurs.

Forward models in fNIRS are approximations to the process of radiation transport. One of the most popular forward models in continuous wave fNIRS due to its utter simplicity is the modified Beer-Lambert law (MBLL).[1] Although the MBLL is most times sufficient for grossly monitoring brain hemodynamics, of course, the human head largely violates the assumption of homogeneity. For stricter reconstructions demands, or better understanding of the image formation process, more elaborated forward models are employed. These forward models, complement the expression of radiation transport with more realistic descriptions of the head anatomy (*anatomical model*) and a more detailed characterization of the optical properties across the different tissues (*optical model*). Often the tern of the radiation transport model, the anatomical model and the optical model are simply collectively referred to as the forward model.

Further author information: (Send correspondence to J.H.V.)
J.H.V.: E-mail: vega@inaoep.mx, Telephone: +522222663100

13th International Conference on Medical Information Processing and Analysis, edited by Eduardo Romero, Natasha Lepore, Jorge Brieva, Juan David García, Proc. of SPIE Vol. 10572, 1057206
 · doi: 10.1117/12.2285918

Scalp blood flow contamination is one of the most pressing issues affecting fNIRS reconstruction. The scalp comes first in the optical path and it is visited twice during the photon migration. The fNIRS community has therefore put forward a number of solutions to account for this undesired contribution including instrumental incorporation of short-distance channels and algorithmic filtering.

We, here, report a new forward model for the estimation of the diffuse reflectance in the adult human head. Previous work has consider only 4 layers scalp, skull, CSF, grey and white matter; here we consider 9 layers. The new model emphasizes the detail considered for the scalp's sublayers, so that attenuation due to scalp blood flow can be characterized for latter incorporation to the reconstruction algorithm (not part of this communication). Radiation transport is solved through Monte Carlo (MC) stochastic modelling. The anatomical description comprises 9 layers including the 5 sub-layers from the scalp. Optical properties are taken from literature reported values, and contributions of hemoglobin species to scalp and gray matter are explicitly modelled. Model's face validity is established here by comparing optimally found modelled remitted spectra against continuous wave broadband fNIRS data, whilst generative parameter vector remains confined to histologically plausible ranges.

2. RELATED WORK: FORWARD MODELLING OF THE HUMAN HEAD

A number of forward models of the human head have been proposed with varying degree of faithfulness depending on their purpose. Purposes varied from assessing the effect of thickness and scattering of certain layer e.g.,[2] or appreciating the fast optical signal e.g.[3] among others. According to their geometrical description of the anatomy, these can be coarsely classified in flat layers models,,[2,4,5] MRI segmented structures[3] and mesh based models.[6] These models often only consider 4 or 5 main tissue layers: scalp, skull, cerebrospinal fluid (CSF), gray matter (GM) and white matter (WM). Diffusion theory e.g,[5] and MC simulations e.g.[3,6] have been popular choices for modelling radiation transport.

3. FORWARD MODEL OF THE HUMAN HEAD

This section describes the three elements of the forward model of the human head proposed in this work.

Radiation transport model Light propagation was simulated using the MC approach. Standard negative exponential distribution was used to determine the free path length, and the Henyey-Greenstein phase function for calculating the direction of the photon following an scattering event.

Anatomical model The proposed anatomical model departs from the mesh model in[6] comprising four tissues: Scalp-Skull, CSF, Gray matter and White matter. This model was refined with *iso2mesh*[7] to deal with the thicknesses of the scalp sub-layers. Tetrahedrons of the refined mesh associated to the scalp were labelled according to the scalp 5 sub-layers by measuring the distance from the scalp surface to interior of the head based on literature reported averaged thicknesses.[8] A section of the final anatomical description is shown in Fig. 1.

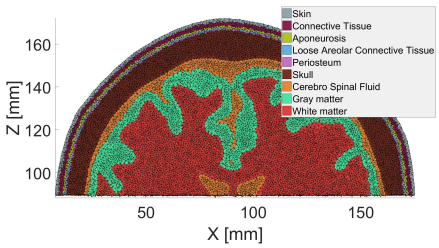

Figure 1. A section of the anatomical model of the human head with the scalp segmented in its five sub-layers; skin, connective tissue, aponeurosis, loose areolar connective tissue and periosteum.

Optical model Each tissue is optically characterized by four parameters, namely; refraction index ($n(\lambda)$), absorption coefficient ($\mu_a(\lambda)$), scattering coefficient ($\mu_s(\lambda)$) and anisotropy factor ($g(\lambda)$). Each parameter was defined for wavelengths between 700 nm to 1000 nm. Optical properties for main human head tissues have been reported in literature: skin,[9] skull,[10] CSF,[2,11] gray matter[12,13] and white matter.[12,13] Linear interpolation was used to compute values at missing wavelengths. We are not aware that optical properties for individual scalp sub-layers has been reported. For these layers, μ_a and μ_s were modelled as a function of their histo-physiological compounds. The optical properties incorporated into the model are summarised in Appendix A.

The final model is understood in terms of the four parameters corresponding to the concentrations of oxigenated and reduced hemoglobin at the scalp and gray matter layers. The model's parameter vector is therefore described by Eq. 1:

$$\pi =< HbO_{2,scalp}, HbR_{scalp}, HbO_{2,brain}, HbR_{brain} > \tag{1}$$

4. MODEL VALIDATION

Face validity of the forward model was established by generating spectra that optimally matches raw experimental broadband measurements from human subjects. The process involves finding the optimal parameters vector for which the model generated spectrum matches a experimental spectrum.

4.1 Experimental spectra

Experimental data used for validation are a subset of those collected by[14] where data from 17 subjects was collected using the continuous wave broadband NIRS system[15] and includes spectra from resting and brain activation states. Measurements were acquired from the pre-frontal cortex at 1, 2 and 3 cm source-detector separation while a memory task was carried out. Following an initial baseline recording of 30 seconds, the stimulus train contained 4 blocks of 30s task stimulus followed by 30s rest period for a total of 9 subperiods. Sensed wavelengths ranged from 770nm to 906nm at 1nm intervals. A full description of the data collection protocol and the instrumentation can be found in the original works.[14,15]

Spectra collected from several of the subjects was affected by detector saturation thus leading to a flat recording. Following visual inspection for data integrity, data from 3 subjects was pick for validation of our forward model (those with qualitatively the cleaner acquired signals). For each subperiod an average spectrum was computed and used as representative spectrum of such subperiod, whether rest or stimulus. These serve as the ground truth for validation. A total of 81 spectra were used (3 subjects $\times$ 9 subperiods $\times$ 3 channels). Figure 2 schematically depicts the samples, the associated stimulus train and the representative spectra.

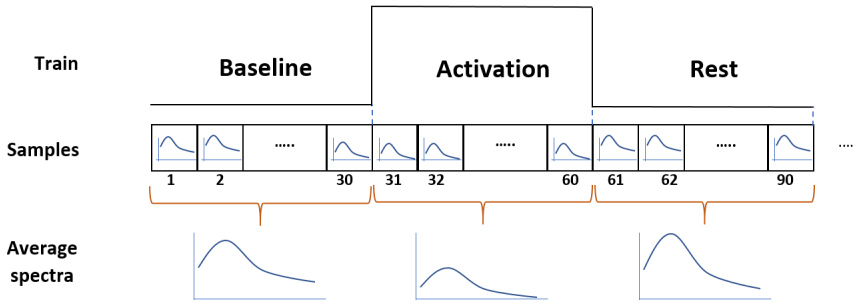

Figure 2. Every point in the sampled data corresponds to a spectrum. The intensity measured in each spectrum is associated to the brain state in function of the experimental stimulus train. The average of spectra in each block is used as ground truth for validation.

4.2 Simulated data

With the described forward model, predicted remitted spectra were generated in MCX[6] by defining the concentration of the four parameters of interest: HbO_2 and HbR both in the scalp and in the brain. The respective concentrations alter the absorption properties of the corresponding layer and hence affecting the remitted spectra at the surface. The broadband experimental dataset contains information at 136 wavelengths. MC is computationally expensive and thus simulations were carried out at wavelengths 784, 800, 818, 835, 851, 868, 881 and 894 nm chosen according to.[16] Synthetic detectors were defined at 1, 2 and 3 cm (euclidean distance) to measure the exiting light mimicking the experimental setup. The synthetic detectors were 1 mm wide and were assumed to accept incoming photon with the same efficiency from all directions. For a more realistic image acquisition simulation, model predicted remitted spectra were convolved with the quantum efficiency of the real sensor.[15] The mesh model was voxelized to be able to run simulations in MCX.[17] MC simulations of 10^8 photons were carried out in 4 GPU's - one GeForce Titan Black, two Tesla M2090 and one Geforce GTX 950.

4.3 Spectra matching optimization

Optimal matching between experimental and simulated diffuse reflectance spectra was found using a genetic algorithm (GA). Individuals were genetically described by the parameter vector in Eq. 1 using a real representation and bounded by physiological ranges derived from[18] (measured in the forehead of 5 subjects) and summarised in Table 1.

Table 1. Absolute Concentration of HbO_2 and HbR in the scalp and brain reported by.[18] Three standard deviations from the mean were used to define the bounds of each parameter in the genetic algorithm.

Parameter	$HbO_{2,scalp}$	HbR_{scalp}	$HbO_{2,brain}$	HbR_{brain}
$\mu \pm \sigma$ $[\mu M]$	12.6 ± 8.97	7.29 ± 4.83	31.0 ± 8.32	19.9 ± 3.67

Population size was set to 15 individuals and initialized randomly. A maximum number of 10 generations was allowed. Mutation rate was set to 0.05 and affected one parameter at a time. Cross-over rate was set to 0.6 and the off-spring maintained half of the genetic code of each parent randomly selected. The top 50% of the population survived to the next generation each time. Fitting was determined by means of the *root mean square error* defined in Eq. 2:

$$RMSE = \left[\frac{1}{N} \sum_{i=1}^{N} (\phi^c - \phi^e)^2 \right]^{1/2} \tag{2}$$

where ϕ^c is the simulated data, ϕ^e is the experimental data and N the number of wavelengths used to simulate the spectra. A good approximation between simulated and measured spectra will support the validity of the model. Note that the physiological parameters used in simulations should be confined to plausible ranges.

5. RESULTS

During the optimization process, a total of 6473 spectra were simulated. The total GA simulation time amounted to 431.5 hours. The percentage of detected photons at each detector in each simulation (from the total injected) corresponds to 0.2%, 0.02% and 0.007% at 1, 2 and 3cm respectively. Figure 3 visually compares the normalised experimental measurement and the optimally selected model generated spectrum. A good correspondence between the curves can be appreciated at all distances.

The final *RMSE* achieved after optimization was: 0.071 ± 0.004, 0.108 ± 0.018 and 0.235 ± 0.015 at the three source-detector separations respectively. Fig. 4 reports the progression of the *RMSE* across the generations of the GA for the different interoptode distances (mean and std. dev. for all the subjects and blocks). Three considerations can be made from Fig. 4:

1. Convergence to optimal solution found happens at different rates. While the bottom curve (spectra at 1cm) shows to converge around 7th generation, the fitting for spectra at 2 and 3cm decrease even at the last generation.

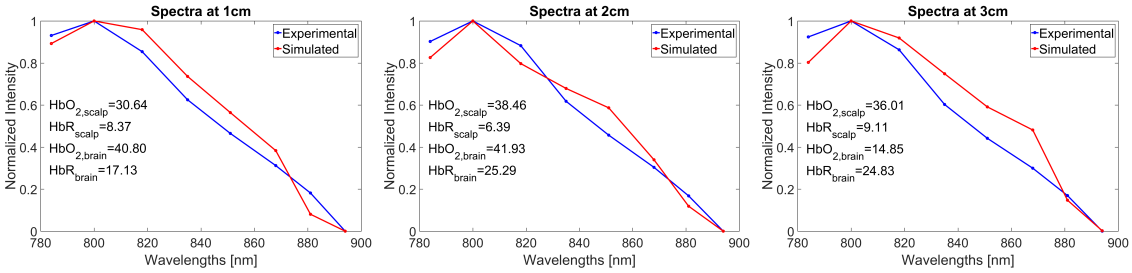

Figure 3. Normalised experimental (blue) and simulated (red) spectra at 1 cm, 2 cm and 3 cm.

2. A different level for each curve can be appreciated which can be partially attributed to the dominance of the scalp parameters at shorter distance (almost making the model be dominated by only 2 instead of 4 parameters in practice), and

3. The standard deviation increases with SD separation. These situations are an effect associated to the number of photons detected at each distance. Despite the severely constraint hyper-parameterization of the GA, and the lack of effort to improve convergence, the fitting achieved yields acceptable spectra.

Fig. 5 shows the distributions of the absolute concentrations recovered for each parameter at the three source-detector separation for the resting and activation states. The values for parameters $HbO_{2,scalp}$, HbR_{scalp} and $HbO_{2,brain}$ remained in the plausible histological ranges. Unfortunately, some values of the parameter HbR_{scalp} reached negative values due to the range allowed in the genetic algorithm. One interesting result can be observed for parameter $HbO_{2,brain}$ where the median show an small increase going from resting to activation states at the 3 cm S-D separations, and the HbR_{brain} show a decrease in agreement with the expected signature of the brain haemodynamics as observed with NIRS in the presence of brain activity. These findings are indicators of the expected behavior of the hemodynamics of functional activation.

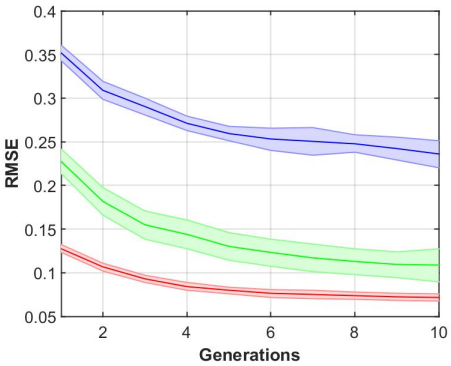

Figure 4. Evolution of the RMSE across the generations of the genetic algorithm for the different interoptode distances: 1, 2 and 3cm [bottom to top]

6. CONCLUSIONS

We have presented and validated a new forward model for the estimation of the diffuse reflectance on the adult human head. The distinctive feature of the new model is its greater attention to the scalp layers as compared to other models reported in literature (see Sect. 2), permitting a good description of the blood content in this outermost tissue. The model generated spectra exhibit a good matching with experimental measurements across different source-detector separations. The model is limited in several ways; for instance blood in the arachnoid is not considered, the optical properties of the skin don't consider the melanin pigment, which is an important absorber of light. Validation can be further improved in several ways; comparisons may be carried out against spectra collected from optical phantoms for which the ground truth is known, spectra correspondence can be

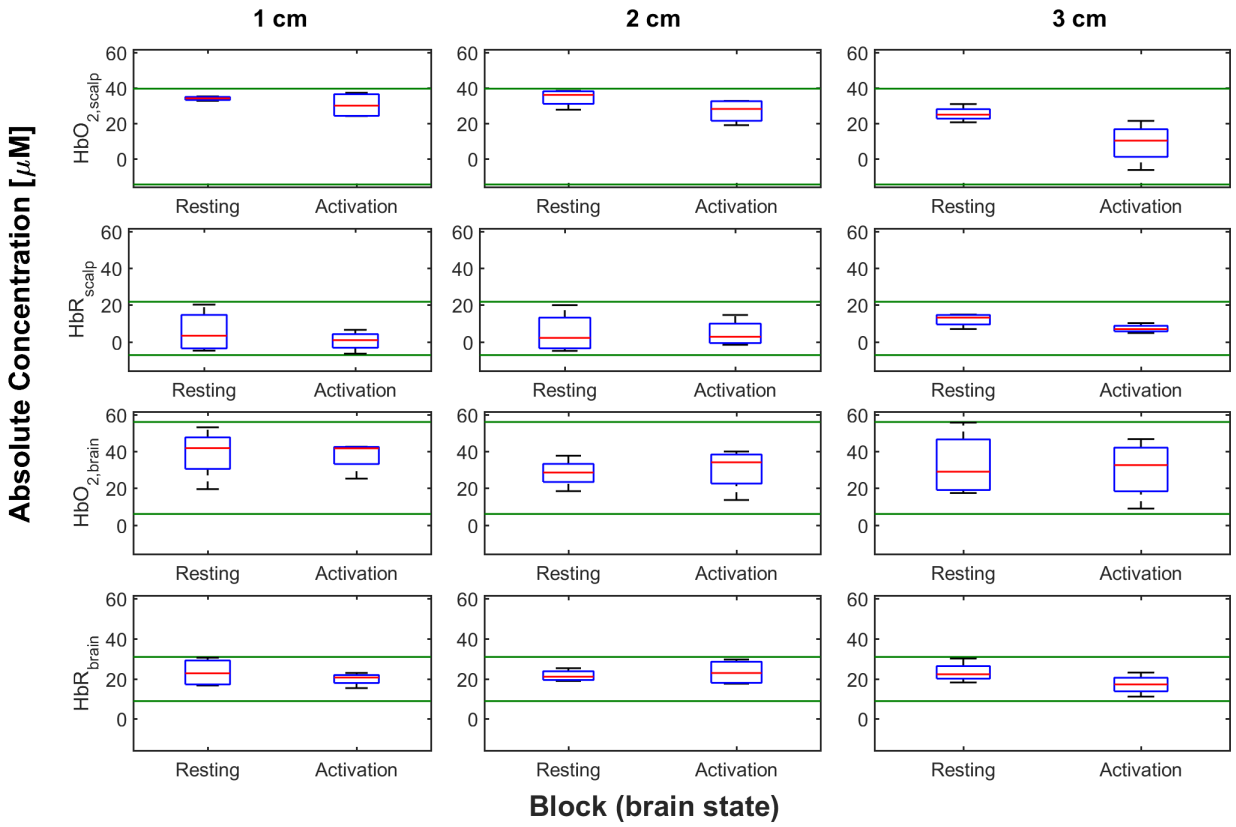

Figure 5. Parameters recovered after optimization at 1, 2 and 3 cm for all the validated spectra. Green lines indicates the minimum and maximum values for each parameter (according to values in table 1).

enhanced through simulations with a larger number of photons and permitting the GA greater exploration of the search space. The developed model will be useful to estimate the diffuse reflectance in function of the hemoglobin changes in the scalp and use this as a priori information in the regularization of the reconstruction process. On the other hand, the realistic anatomical structure and optical model improves the estimated reflectance and may reduce the convergence rates in based-model reconstruction methods.

Future work splits in two major branches. First, enriching the model for considering the cytochrome-c-oxydase. Second, by using the forward model for addressing the confounding effect of scalp blood flow contribution during the image reconstruction stage.

REFERENCES

[1] Delpy, D. T., Cope, M., van der Zee, P., Arridge, S., Wray, S., and Wyatt, J., "Estimation of optical pathlength through tissue from direct time of flight measurement," *Physics in medicine and biology* **33**(12), 1433 (1988).

[2] Okada, E. and Delpy, D. T., "Near-infrared light propagation in an adult head model. ii. effect of superficial tissue thickness on the sensitivity of the near-infrared spectroscopy signal.," *Appl. Opt.* **42**, 2915–222. (Jun 2003).

[3] Franceschini, M. A. and Boas, D. A., "Noninvasive measurement of neuronal activity with near-infrared optical imaging," *Neuroimage* (2004).

[4] Okada, E. and Delpy, D. T., "Near-infrared light propagation in an adult head model. i. modeling of low-level scattering in the cerebrospinal fluid layer.," *Appl. Opt.* **42**, 2906–214. (Jun 2003).

[5] Correia, T., Gibson, A., and Hebden, J., "Identification of the optimal wavelengths for optical topography: a photon measurement density function analysis," *Journal of Biomedical Optics* **15**, 056002 (2010).

[6] Fang, Q., "Mesh-based monte carlo method using fast ray-tracing in plucker coordinates," *Biomed. Opt. Express* **1**, 165–175 (2010).

[7] Fang, Q. and Boas, D. A., "Tetrahedral mesh generation from volumetric binary and grayscale images," in [*Biomedical Imaging: From Nano to Macro, 2009. ISBI'09. IEEE International Symposium on*], 1142–1145, IEEE (2009).

[8] Hiroyuki Hori, Giuseppe Moretti, A. R. and Crovato, F., "The thickness of human scalp: Normal and bald," *Journal of Investigative Dermatology* **58**, 396?399 (1972).

[9] Simpson, R. C., Kohl, M., Essenpreis, M., and Cope, M., "Near-infrared optical properties of ex vivo human skin and subcutaneous tissues measured using the Monte Carlo inversion technique," *Phys. Med. Biol.* **43**, 2465–2478 (1998).

[10] Bashkatov, A. N., Genina, E. a., Kochubey, V. I., and Tuchin, V. V., "Optical properties of human cranial bone in the spectral range from 800 to 2000 nm," *Proc. SPIE 6163, Saratov Fall Meet. 2005 Opt. Technol. Biophys. Med. VII* **6163**, 616310–616310–11 (Aug. 2006).

[11] Custo, A., Wells, W. M. I., Barnett, A. H., Hillman, E. M. C., and Boas, D. A., "Effective scattering coefficient of the cerebral spinal fluid in adult head models for diffuse optical imaging," *APPLIED OPTICS* **45**, 4747 – 4755 (July 2006).

[12] Van Der Zee, P. and Essenpreis, M., "Optical properties of brain tissue," *Proc. SPIE 1888, Phot. Migr. Imaging Random Media Tissues* , 454–465 (1993).

[13] Vo-Dinh, T., [*Biomedical Photonics Handbook: Biomedical Diagnostics*], vol. 2, CRC press (2014).

[14] de Roever, I., Bale, G., Cooper, R. J., and Tachtsidis, I., "Cytochrome-c-oxidase exhibits higher brain-specificity than haemoglobin in functional activation," in [*Optics and the Brain*], BTh4D–4, Optical Society of America (2016).

[15] Bale, G., Mitra, S., Meek, J., Robertson, N., and Tachtsidis, I., "A new broadband near-infrared spectroscopy system for in-vivo measurements of cerebral cytochrome-c-oxidase changes in neonatal brain injury," *Biomedical Optics Express* (5) (2014).

[16] Arifler, D., Zhu, T., Madaan, S., and Tachtsidis, I., "Optimal wavelength combinations for near-infrared spectroscopic monitoring of changes in brain tissue hemoglobin and cytochrome c oxidase concentrations," *Biomedical Optics Express* **6**(3), 933–947 (2015).

[17] Fang, Q. and Boas, D. A., "Monte carlo simulation of photon migration in 3d turbid media accelerated by graphics processing units," *Opt. Express* **17**, 20178–20190 (2009).

[18] Louis Gagnon, Claudine Gauthier, R. D. H. F. L. J. S. and Boas, D. A., "Double-layer estimation of intra- and extracerebral hemoglobin concentration with a time-resolved system," *Journal of Biomedical Optics* **13** (2008).

[19] Jacques, S. L., "Corrigendum: Optical properties of biological tissues: a review," *Phys. Med. Biol.* **58**, 5007–5008 (July 2013).

[20] Dizem Arifler, Ina Pavlova, A. G. and Richards-Kortum, R., "Light scattering from collagen fiber networks: Micro-optical properties of normal and neoplastic stroma," *Biophys J.* **92**(9), 3260?3274. (2007).

[21] Fisher, B. T. and Hahn, D. W., "Measurement of small-signal absorption coefficient and absorption cross section of collagen for 193-nm excimer laser light and the role of collagen in tissue ablation," *APPLIED OPTICS* **43**(29), 5443–5451 (2004).

[22] Bashkatov, A. N., Genina, E. a., and Tuchin, V. V., "Optical properties of skin, subcutaneous, and muscle tissues: a review," *J. Innov. Opt. Health Sci.* **04**, 9–38 (Jan. 2011).

[23] Yaroslavsky, A., Schulze, P., Yaroslavsky, I., Schober, R., Ulrich, F., and Schwarzmaier, H., "Optical properties of selected native and coagulated human brain tissues in vitro in the visible and near infrared spectral range," *Phys Med Biol* **47**, 2059–73. (2002).

[24] D. L. Collins, A. P. Zijdenbos, V. K. J. G. S. N. J. K. C. J. H. and Evans, A. C., "Design and construction of a realistic digital brain phantom," *IEEE Trans. Med. Imaging* **17**(3), 463?468 (1998).

APPENDIX A. OPTICAL PROPERTIES OF THE TISSUE LAYERS

Table 2. Definition of the optical parameters of the model layers

Layer	Parameters	Values (Source)
Skin	$n(\lambda)$	1.37[11]
	$\mu_a(\lambda)$	Simpson et al.[9]
	$\mu_s(\lambda)$	Simpson et al.[9]
	$g(\lambda)$	Ranging from 0.7 to 0.9[19]
	d	1668 μm[8]
Connective tissue	n	1.37[11]
	$\mu_a(\lambda)$	$\mu_a(\lambda) = \mu_a^{CT}(\lambda) + C_{HbO_2} * \mu_a^{HbO_2} + C_{HHb} * \mu_a^{HHb}$
	$\mu_s(\lambda)$	$\mu_s(\lambda) = C_{collagen} * \mu_s^{collagen}(\lambda)$
	$g(\lambda)$	0.9[20]
	d	1801 μm[8]
Aponeurosis	$n(\lambda)$	1.37[11]
	$\mu_a(\lambda)$	Fixed to value reported by[21]
	$\mu_s(\lambda)$	$\mu_s(\lambda) = C_{collagen} * \mu_s^{collagen}(\lambda)$
	$g(\lambda)$	0.9[20]
	d	1000μm[8]
Loose areolar CT	$n(\lambda)$	1.37[11]
	$\mu_a(\lambda)$	Fixed to value reported in[21]
	$\mu_s(\lambda)$	$\mu_s(\lambda) = C_{collagen} * \mu_s^{collagen}$
	$g(\lambda)$	0.9[20]
	d	500 μm
Periosteum	$n(\lambda)$	Fixed to 1.37
	$\mu_a(\lambda)$	Fixed to value reported by[21]
	$\mu_s(\lambda)$	$\mu_s(\lambda) = C_{collagen} * \mu_s^{collagen}$
	$g(\lambda)$	0.9[20]
	d	500 μm
Skull	n	1.42[11]
	$\mu_a(\lambda)$	Range [0.012 - 0.028 mm^{-1}][22]
	$\mu_s(\lambda)$	Range [5.71 - 9.19 mm^{-1}][22]
	$g(\lambda)$	Range [0.702 - 0.96][23]
	d	According to the anatomical model[6]
CSF	$n(\lambda)$	1.37[11]
	$\mu_a(\lambda)$	Range [4e-4 - 2e-4 mm^{-1}][10]
	$\mu_s(\lambda)$	Range [0.01-1.855 mm^{-1}][10]
	$g(\lambda)$	Range [0.9 - 0.92][10]
	d	According to the anatomical model[24]
Gray matter	$n(\lambda)$	1.37[11]
	$\mu_a(\lambda)$	Model of Correia et al.[5]
	$\mu_s(\lambda)$	Range [6.63 - 8.81 mm^{-1}][23]
	$g(\lambda)$	Range [0.89 - 0.9][23]
	d	According to the anatomical model[24]
White matter	$n(\lambda)$	1.38[11]
	$\mu_a(\lambda)$	Range [0.07 - 0.1084 mm^{-1}][23]
	$\mu_s(\lambda)$	Range [33.9 - 41.64 mm^{-1}][23]
	$g(\lambda)$	Range [0.84 - 0.88][23]
	d	According to the anatomical model[24]